Flux effect on defect evolution in uranium dioxide under electronic and ballistic regime

Gaelle Gutierrez, Marion Bricout, Laurent Roux, Claire Onofri-Marroncle

Flux effect on defect evolution in uranium dioxide under electronic and ballistic regime

G. Gutierrez[1], M. Bricout[1], L. Roux[1], C. Onofri[2]*

[1] Université Paris-Saclay, CEA, Service de recherche en Corrosion et Comportement des Matériaux, SRMP, F-91191 Gif-sur-Yvette, France.

[2] CEA, DES, IRESNE, DEC, Cadarache, F-13108 St Paul lez Durance, France

Abstract

The microstructure evolution of ion-irradiated UO_2 was evaluated by *in situ* Raman spectroscopy. Transmission electron microscopy (TEM) for selected irradiation conditions were also conducted. The UO_2 samples were irradiated with single- (900 keV I ions) or dual-ion beam (900 keV I and 27 MeV Fe or 36 MeV W ions) with different ratio between the high- and low-velocity ion fluxes (R). The analysis of the damage build-up shows that the electronic excitations deposited by the high-velocity ions affect the formation and the evolution of defects induced by the nuclear energy loss. In addition, the kinetics of dislocations evolution are all the more advanced as the flux ratio is favourable to the electronic excitations. Thus, the greater R is, the more electronic excitations are favoured and the more the microstructure evolves.

Keywords: Uranium dioxide, in situ Raman, TEM, defects, dislocations, Ionization, dual ion beam irradiation

*Corresponding author

E-mail: gaelle.gutierrez@cea.fr

Introduction

During ion irradiations, the incident particle interacts with the nuclei and electrons of the atoms of the matrix. Its slowing down in the matter occurs through electronic or nuclear energy losses, with a proportion of each varying, depending on the ion velocity. As a result of these energy losses in the material, ballistic damage and/or electronic excitations/ionizations take place. These phenomena can thus be coupled and are not independent. The electronic excitations can influence ballistic damage inducing an evolution of the microstructure. Depending on the material, the electronic excitations coupled with ballistic damage lead to various phenomena. Charged particles can promote healing of pre-existing defects in the structure or prevent the generation of defects like in SiC, Si or GaAs [1-4]. Through local heating along the ion trajectory, a significant reduction of disorder can occur, impacting not only at the microscopic scale but also potentially influencing macroscopic properties, particularly mechanical ones [5]. On the contrary, nuclear and electronic damages may accumulate, enhancing disorder in the material as observed in STO, KTO or AlN [6-8]. In silicon single-crystals, it was highlighted that the ratio of the high- to low-velocity ion fluxes induces a modification of the remaining disorder during dual-beam irradiations [1]. In summary, the coupling between electronic or nuclear energy losses is not a straightforward addition of the two beam effects.

In uranium dioxide (UO_2), the standard fuel for pressurized water reactors, the separate effects of nuclear and electronic energy losses were extensively studied. After irradiations in the nuclear energy-loss regime, point defects are formed inducing, with the fluence increase, the formation of dislocation loops and vacancy objects [9-14]. The loop then evolve into dislocation lines. High-energy ion irradiations induces the formation of continuous ion tracks along the ion paths (between 22 and 29 keV/nm) [15-18]. The coupling between the nuclear and electronic energy losses induces a microstructure evolution compared to the sole irradiation with low-velocity ions. Due to the electronic ionizations, during dual-beam irradiations, the point defects could be more mobile inducing the growth of dislocation loops through the absorption of interstitial-type defects [19-21] and a stress relaxation [21]. For an electronic energy loss close to the threshold of the track formation, a possible synergetic effect between the ballistic damage and the intense electronic ionizations was revealed by a stress increase [18]. The level of electronic energy loss is thus a key parameter in these energy dissipation processes [22]. In addition, it is worth stressing that the dislocation population is different for a similar low-energy ion fluence after a sequential or a simultaneous irradiation. Indeed, after a sequential irradiation, only dislocation loops are observed, on contrary to, after a simultaneous irradiation, where dislocations lines are already formed. The ratio between the implanted low- and high-energy ions is then a key parameter in these coupling effect.

The aim of the present paper is to characterize the flux influence of the high-energy ions on the defect evolution. For this purpose, we used a multi-beam irradiation facility coupling with *in situ* Raman spectroscopy measurements. Observations with transmission electron microscopy (TEM) were also carried out after irradiation at the final fluence step. We show that the ionizations modify the ballistically-induced defects depending on the ratio between the electronic and ballistic energy losses.

Experimental methods

UO_2 polycrystalline samples with an average grain size of 7.6 µm and a density of 10.74 g.cm^{-3} were prepared at the 'Laboratoire UO_2' facility at CEA Cadarache. The samples were mirror polished then annealed at 1700°C during 24 h under an Ar-H_2 (5%) atmosphere. An additional polishing step was added to remove the deepening effect of grain boundaries with colloidal silica suspension. A final annealing step at 1400°C during 4 h under Ar-H_2 (5%) was performed.

The irradiations were performed at JANNuS-Saclay facility under a vacuum lower than 10^{-7} mbar in order to prevent any oxidation [23]. To study the synergistic effects between nuclear and electronic energy losses, several irradiation sequences were carried out : (1) a single irradiation with a low-velocity (i.e., 900 keV I, referred as S_n) ion beam, (2) sequential irradiations with a low-velocity (i.e., 900 keV I, referred as S_n) then a high-velocity (i.e., 27 MeV Fe or 36 MeV W, referred as S_e) ion beams, referred to as $S_n + S_e$, or (3) simultaneous irradiations with a low-velocity (S_n) and high-velocity (S_e) ion beams, referred to as S_n & S_e (Tab. 1).

Sample denomination	Irradiation sequence	Final I fluence (10^{14} cm^{-2})	Final Fe/W fluence (10^{14} cm^{-2})	R = Φ_{ele}/ Φ_{nuc}
S_n	900 keV I	10	-	
$S_{n\ E13} + S_e$	900 keV I then 27 MeV Fe	0.1	5	
$S_{n\ E15} + S_e$	900 keV I then 36 MeV W	10	5	
S_n & S_e R_{low}	0.9 MeV I and 36 MeV W	5	2	0.4
S_n & S_e R_{high}	0.9 MeV I and 27 MeV Fe	4	8	2

Table 1: Irradiations conditions: the irradiation sequence, the final ion fluences and the flux ratio between the high- and low-velocity ions (R) for the dual-ion beam irradiations.

For the sequential irradiations, two S_n pre-damaged level were used: at a fluence of 10^{13} cm^{-2} ($S_{n\ E13} + S_e$) and of 10^{15} cm^{-2} ($S_{n\ E15} + S_e$). In addition, the ratio between the high- and low-velocity ion fluxes (R) during the dual-ion beam irradiations (S_n & S_e) was monitored. For all the irradiations, the high-velocity ion flux was maintained below 1 × 10^{11} cm^{-2}.s^{-1} to minimize the samples beam heating. The samples temperature was controlled with a thermocouple and a thermal camera.

The nuclear energy loss of the 0.9-MeV I ions was calculated with the Iradina code [24] with displacement energies of 40 eV for U and 20 eV for O atoms. The replacement energy was stated at the lattice energy (E_{latt}) to compare with the data from the literature [18]. The projected range (R_p) is estimated at 0.16 µm. The electronic and nuclear energy losses of the 36-MeV W and 27-MeV Fe ions were also determined. At the surface, the nuclear energy loss is negligible and the electronic energy losses, evaluated at 13.0 keV.nm^{-1} for 36-MeV W and at 12.2 keV.nm^{-1} 27-MeV Fe ions, are closed for the two ions. In addition, the R_p of S_e ions is estimated at 3.5 and 3.8 µm for 36-MeV W and 27-MeV Fe ions, respectively, which is far larger than the implantation depth of 0.9-MeV I ions. Thus, in the region where the S_e and S_n ions interact, the electronic energy loss of the S_e ions is predominant.

In situ Raman measurements were performed during the irradiations (experimental set up described in [25]). Raman analyses using an Invia Reflex Renishaw spectrometer coupled with a frequency-doubled Nd:YAG (532 nm) laser and a 2400 groove / mm grating were performed in broad wave-number range between 200 and 1400 cm^{-1}. The effective laser penetration depth d can be estimated to ~1 µm for our analysis conditions [26]. *In situ* Raman spectra were recorded after the ion beam shut off during 120 s at each step of irradiation fluence. The accuracy on band position deduced from the spectrum simulation is estimated at ± 1 cm^{-1}.

Transmission Electron Microscopy (TEM) observations were performed with a Thermo Scientific Talos F200X TEM operating at 200 kV at the LECA (Laboratoire d'Examens des Combustibles Actifs) in CEA Cadarache. Electron-transparent cross sectional thin foils were prepared by the Focused Ion Beam (FIB) technique at CP2M (Centre Pluridisciplinaire de Microscopie électronique et de Microanalyse) in Marseille.

Results

Sequential irradiations (S_n + S_e)

The sequential irradiation (S_n + S_e) consists to irradiate firstly with low-energy ions (S_n) then with high-energy ions (S_e). The damage build-up evolution during each irradiation sequence was followed by *in situ* Raman measurement. Figure 1 gathers examples of *in situ* Raman spectra recorded during the first sole S_n irradiation of a UO_2 sample at several ion fluences. Before irradiation, the triply degenerated Raman (T_{2g}) active mode at 445 cm^{-1}, typical of the fluorite-type structure, is shown [27]. A peak with a weak intensity is also observed at ~570 cm^{-1} associated to the Raman inactive vibration mode T1u-LO (referred as LO) which is particularly marked due to a resonance effect with the laser used (532 nm) [28, 29]. The LO band is a Raman-forbidden mode in the perfect fluorite-type structure, becoming active with the presence of defects due to a breakdown in the selection rules. In addition, at 1150 cm^{-1}, a very intense peak attributed to the 2 T1u LO mode (referred as 2LO) is also present on the Raman spectra [30]. With the increase of the irradiation fluence, the T_{2g} band broadens and its intensity decreases correlated with an increase of the LO band intensity and a decrease of the 2LO band. In addition, two other bands in the 500-700 cm^{-1} range denoted by U1 (~530 cm^{-1}) and U3 (~630 cm^{-1}) are observed. The increase of U1, U3 and LO bands intensity is associated to the formation of atomistic defects in the UO_2 crystal [31-35]. After an irradiation fluence of 1 × 10^{14} cm^{-2}, no more Raman spectra evolution is observed.

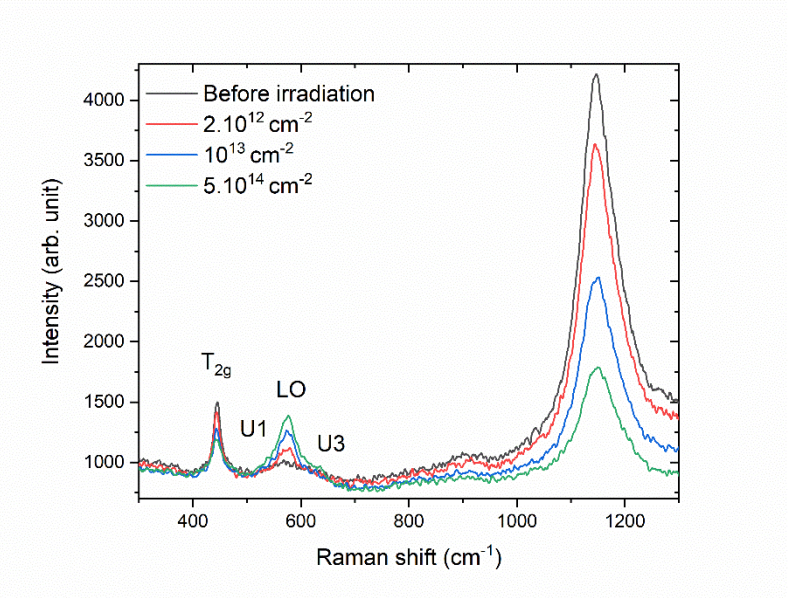

Figure 1: In situ Raman spectra recorded on a UO_2 sample irradiated with S_n ions (900 keV I) at different irradiation fluences.

To compare the different damage build-up kinetics obtained by *in situ* Raman, a Raman spectra fitting was performed by using pseudo-Voight function in the range of 300 to 700 cm^{-1}. It is difficult to decorrelate the evolutions of each band separately (U1, LO and U3) with a good precision. As all these bands are linked to the defect formation, we have followed the evolution of band area sum (U1+LO+U3) referred as U, highlighting a global damage evolution. The normalized U area is represented in Fig. 2 as a function of the S_n ion fluence for the low-energy ion irradiation. No significant evolution is observed for the lower S_n fluence before 3×10^{12} cm^{-2}. Then, a continuous increase of the U area occurs with the fluence up to around 1×10^{14} cm^{-2}. For higher fluences, a signal stabilization is shown.

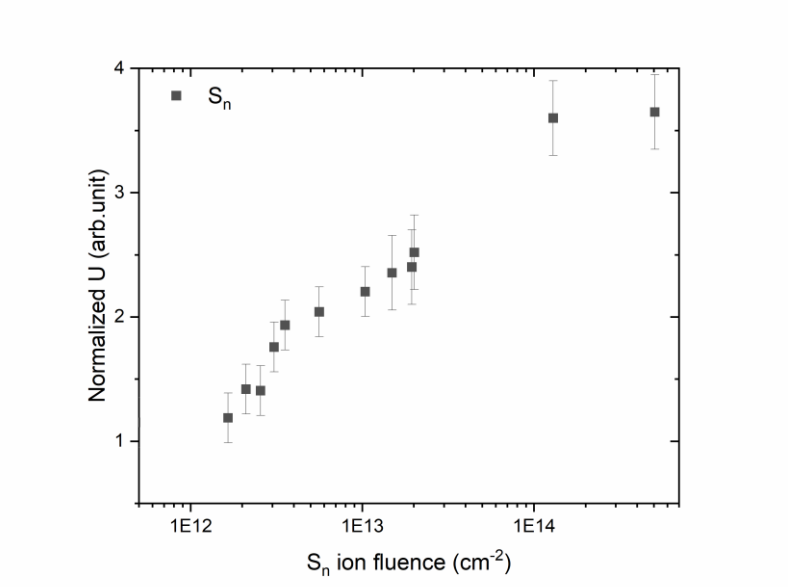

Figure 2: Damage build-up kinetics obtained by in situ Raman: variations of the normalized U band area for UO_2 samples during the S_n irradiation.

The sequential irradiation with S_e ions induces a modification of the Raman spectra for the pre-damaged UO_2 samples irradiated at a low ($S_{n\ E13}$ + S_e) or high ($S_{n\ E15}$ + S_e) S_n ion fluence. This change is highlighted by a decrease of the U area (Fig. 3). No significant evolution is observed for the lower S_e fluences up to ~ 2×10^{12} cm^{-2} for the both initial damage levels. Then, a decrease of the U area occurs with the S_e fluence up to around 4×10^{13} and 7×10^{13} cm^{-2} for $S_{n\ E13}$ + S_e and $S_{n\ E15}$ + S_e, respectively. For higher fluences, a signal stabilization is shown for the two irradiations. Thus, a similar global evolution is observed as function as the S_e fluence but with different level of U value stabilization at 1.2 and 2.8 for $S_{n\ E13}$ + S_e and $S_{n\ E15}$ + S_e, respectively.

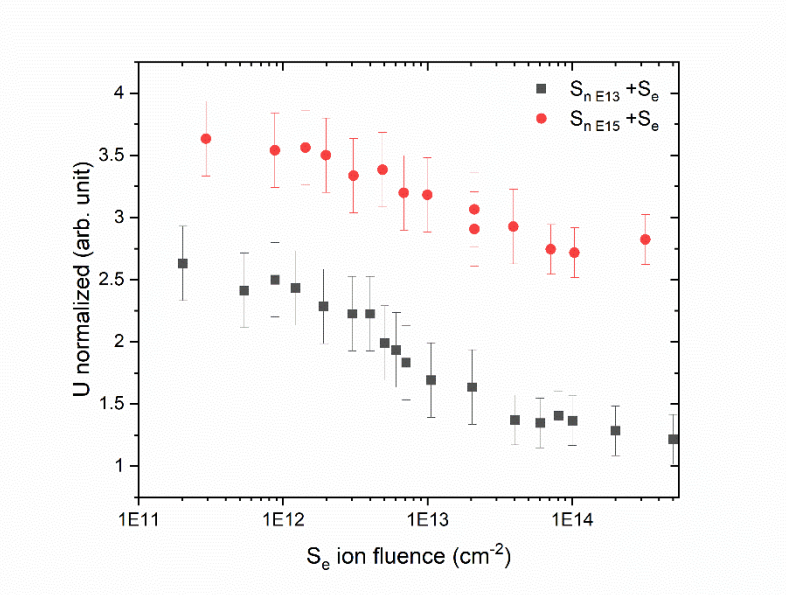

Figure 3: Damage build-up kinetics obtained by in situ Raman: variations of the normalized U band area for UO_2 samples during the S_n + S_e irradiations.

Simultaneous irradiations (S_n & S_e)

The different damage build-up kinetics obtained by *in situ* Raman for the dual-ion beam irradiations are compared to the one determined for the sole S_n irradiation as a function of the S_n ion fluence (Fig. 4). We observed an evolution of the U bands at a lower fluence for the samples submitted to the S_n & S_e irradiations. Indeed, the U value increases after 10^{12} cm^{-2} for the S_n & S_e (R_{low} and R_{high}) whereas, for the S_n, the increase is seen at 3×10^{12} cm^{-2}. For all the conditions, the intensity of the U bands reaches a maximum value but at different fluences. The maximum intensity of the U bands, with respect to the uncertainty, is achieved at 3.6, 3.4 and 2.7 after a fluence of around 1×10^{14}, 5×10^{13} and 1×10^{13} cm^{-2} for the S_n, S_n & S_e with R_{low} and R_{high} irradiations, respectively. For the S_n & S_e irradiations, this maximum is followed by a U area decrease and a stabilization at lower value at around 3.1 and 1.9 for the R_{low} and R_{high}, respectively.

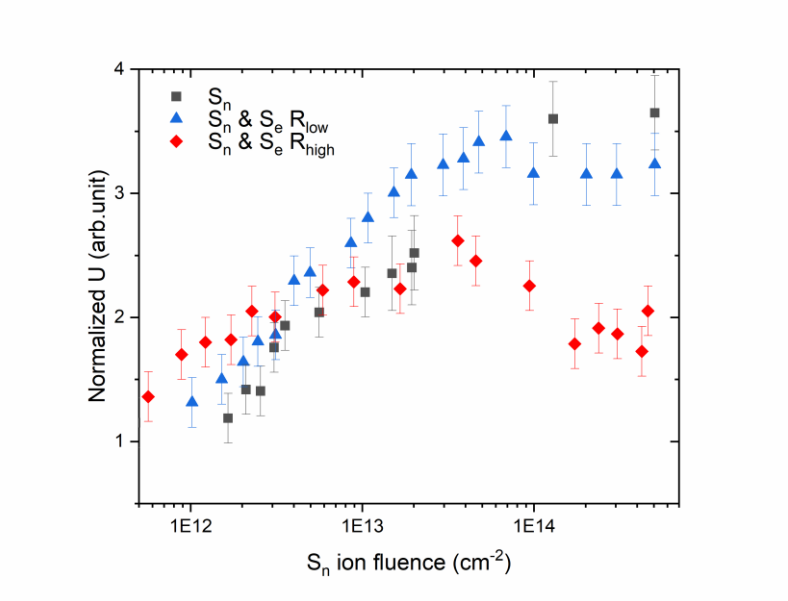

Figure 4: Damage build-up kinetics obtained by in situ Raman: variations of the normalized U bands area for UO_2 samples during the S_n, S_n & S_e R_{low} and S_n & S_e R_{high} irradiations.

Cross-sectional TEM lamella were observed after the different irradiation sequences (S_n or S_n & S_e) to characterize the extended defects when the Raman signal is stabilized. Because of the FIB preparation, the defects induced at low fluences, which are few in number, are not observable because the defects induced by the preparation are more numerous. Thus, after an irradiation at 4×10^{14} cm^{-2} with the low-energy ion (S_n), no significant changes were observed compared to the unirradiated sample due to the FIB lamella preparation [22]. For a higher S_n ion fluence (7×10^{14} cm^{-2}), we observed the presence of numerous small dislocation loops (Fig. 5.a-b). The S_n & S_e ion irradiations (at 4-5 $\times 10^{14}$ cm^{-2} for the S_n ion fluence) induce a microstructure evolution compared to the sole S_n irradiation (for a S_n fluence of 4 and 7×10^{14} cm^{-2}) (Fig. 5.c-f). After the S_n & S_e R_{low} irradiation, the dislocation loops grow compared to the sole S_n microstructure which exhibits mainly smaller loops even at higher S_n ion fluence. With the flux ratio increase, dislocation lines, induced by the larger loop interactions, start to appear [12, 36]. Note that no vacancy objet growth was observed for all the irradiations at an equivalent S_n ion fluence. Thus, the microstructure observations by TEM highlight different dislocation populations.

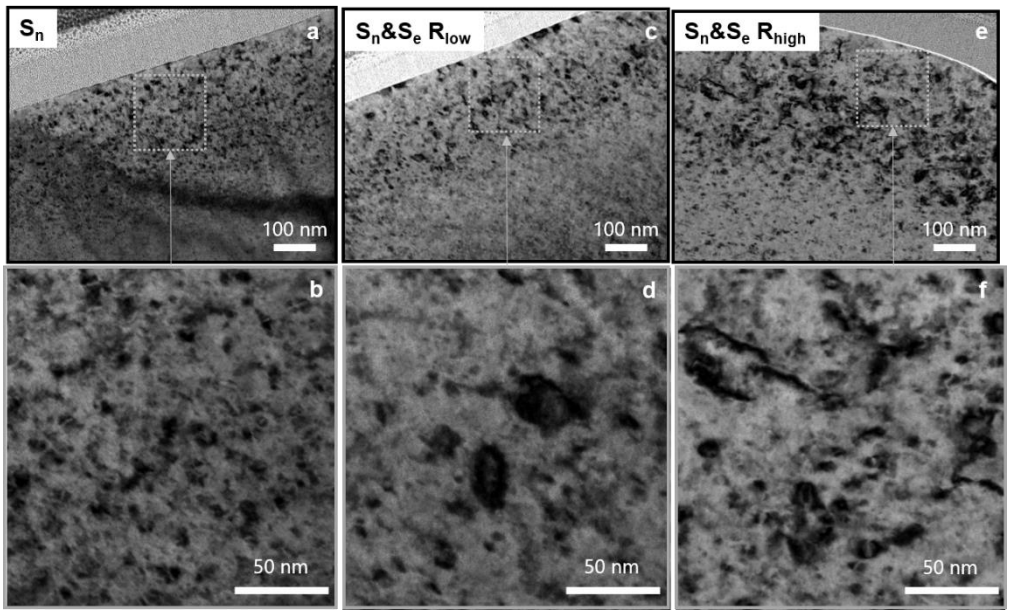

Figure 5: Bright field TEM micrographs of UO_2 samples after the (a-b) S_n irradiation at 7 × 10^{14} cm^{-2}, the S_n & S_e irradiations with (c-d) R_{low} at 5 × 10^{14} and 2 × 10^{14} cm^{-2} and (e-f) with R_{high} at 4 × 10^{14} and 8 × 10^{14} cm^{-2} for the low- and high energy ions, respectively. The diffraction vector is along <200>.

The dislocation loop size distribution is presented in Fig. 6 for the S_n irradiation at 7 × 10^{14} cm^{-2} and the S_n & S_e irradiations with R_{low} at 5 × 10^{14} and 2 × 10^{14} cm^{-2}, for the low- and high energy ions, as well as with R_{high} at 4 × 10^{14} and 8 × 10^{14} cm^{-2} for the low- and high energy ions. The S_n & S_e R_{low} irradiation induces a decrease of the smaller loop population (< 3 nm) to the benefit of the loops with higher sizes (> 3 nm). The evolution is even more pronounced for the S_n & S_e R_{high} irradiation. Thus, on contrary to the sole S_n irradiation where no dislocations larger than 6 nm are formed, the S_n & S_e irradiations induces the apparition of larger loops (> 6 nm).

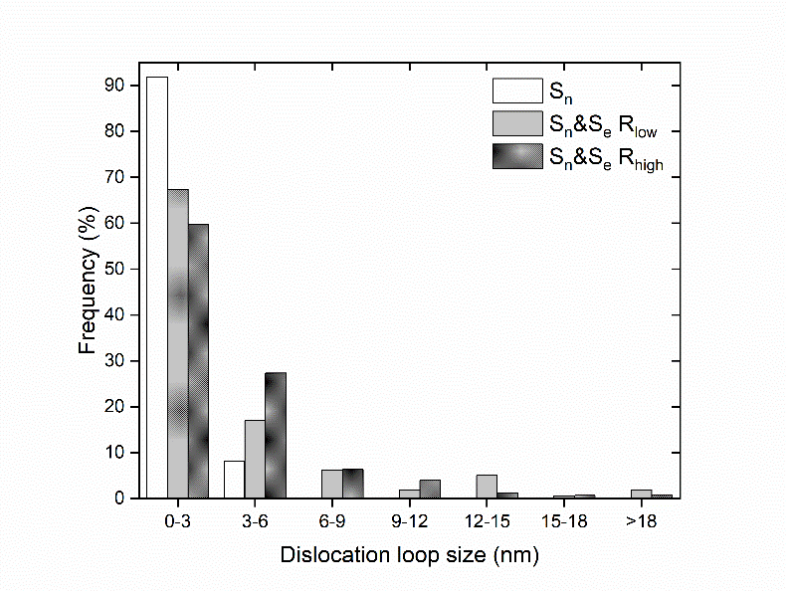

Figure 6: Size distribution of the dislocation loops in the UO_2 samples for the sole S_n irradiation at a fluence of 7 × 10^{14} cm^{-2}, the S_n & S_e irradiations with R_{low} at 5 × 10^{14} and 2 × 10^{14} cm^{-2} and with R_{high} at 4 × 10^{14} and 8 × 10^{14} cm^{-2} for the low- and high energy ions, respectively.

Discussion

Effect of the initial damage level on the damage build-up evolution: sequential irradiation (S_n + S_e)

The S_e ions irradiation induces a modification of the Raman spectra for the pre-damaged UO_2 samples. To directly compare the U evolution for the two sequential irradiations ($S_{n\ E13}$ + S_e and $S_{n\ E15}$ + S_e), the ratio between the U value before (sole S_n irradiation) and after the S_e irradiation (S_n + S_e) is represented as function as the S_e fluence (Fig. 7).

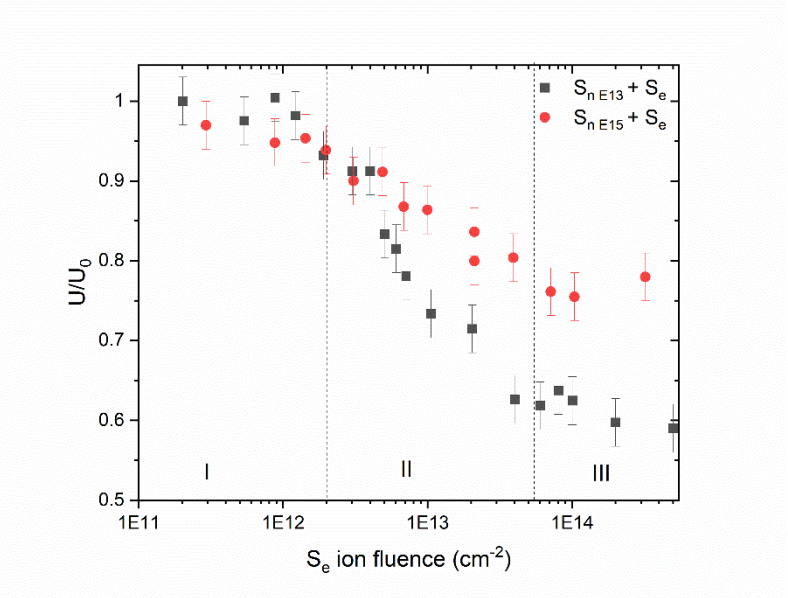

Figure 7: Normalized area U bands: ratio between the U band area for UO_2 samples irradiated before and after the S_e irradiations ($S_{n\ E13}$ + S_e or $S_{n\ E15}$ + S_e).

This U ratio is linked to the disorder evolution induced by the electronic excitations. The two kinetics evolve in the same way: I) up to 2 x 10^{12} cm^{-2}, no change is observed, II) then a decrease in the U signal occurs and, finally, III) from 4 x 10^{13} cm^{-2} the signal is stable. The decrease of the U area is correlated with an evolution of the extended defects. Indeed, after the S_e irradiation of a S_n pre-damaged sample at 7 × 10^{14} cm^{-2}, the loop density decreases and their size increases, highlighting a dislocation loop growth under electronic ionizations [22]. The Raman signal evolution is likely a consequence of the defects, maybe related to the uranium and oxygen interstitials/point defects, recombination and/or clustering [34]. Thus, for the step I, the electronic ionizations affect only a small part of the pre-existing defects (for a thermal spike radius of 3 nm [22], around 25 % of the surface is irradiated by the S_e ions at 10^{12} cm^{-2}). With the increase of the S_e fluence (II), more thermal spikes are induced on the microstructure, leading to a more important recombination/clustering of pre-existing defects. This results in a decrease in the U signal, coupled with an accelerated growth of the dislocation loops. The following signal stabilization (III), occurring at a similar S_e fluence no matter the pre-damaged level, may indicate

that, from this fluence, the defects, affected by this level of electronic excitations, have already interacted with the S_e ions.

In addition, depending on the initial level of damage, the electronic ionizations seems to be more or less efficient. Indeed, the stabilization is achieved at a value of fractional recovery around 0.60 and 0.75 for the $S_{n\,E13}$ + S_e or $S_{n\,E15}$ + S_e, respectively. After a S_n ion fluence of 10^{13} or 10^{15} cm^{-2}, different defect populations, such as point or extended defects, are generated in the microstructure. For the pre-damage level at 10^{13} cm^{-2}, only few dislocation loops are formed, their density is very low [36]. The majority of defects are point defects or small defect clusters. The deposited energy after the passage of the high-energy ions on this microstructure will favour their migration. A defect recombination/clustering then occurs inducing a loop dislocation growth and a subsequent decrease of interstitials concentration [37]. After a S_n ions irradiation at a fluence of 10^{15} cm^{-2}, more dislocations loops are formed, maybe even few lines are already present. The S_e ions will also induce a thermal spike along their path resulting to the defect migration. However, as the dislocations growth is more advanced, less interstitials are available for the recombination. In addition, the already formed dislocation loops may act as a sink for the interstitials. The interstitial absorption on existing loops may then be favoured over the defect recombination. Thus, the relative disorder evolution will be smaller for the higher level ($S_{n\,E15}$ + S_e) compared to one at lower level ($S_{n\,E13}$ + S_e).

Influence of the ratio of the high- to low-velocity ion fluxes on the microstructure evolution

A significant effect of the electronic energy dissipation on the radiation-induced defect evolution was shown with a strong dependence on the ratio between the high- and low-velocity ion fluxes (R) during the dual-ion beam irradiations (Fig. 8). For a maximum S_n fluence of 4×10^{14} cm^{-2}, we observe that the kinetics of dislocations evolution are all the more advanced as the flux ratio is favourable to the electronic excitations. This observation is coupled with a greater decrease of the U signal as the flux ratio increases.

A closer comparison of damage build-up kinetics shows different stages depending on the irradiation conditions (S_n or S_n & S_e). To compare this signal evolution, we used the Multi-Step Damage Accumulation (MSDA) model [38]. In this model, the damage accumulation may occur in one, two or more steps described by the following equation:

$$D = \sum_{i=1}^{n-1} \left\{ D_i^{sat}\ G\left[1-\exp(-\sigma_i(\Phi-\Phi_i))\right] \prod_{k=1}^{n} \left[\exp\left(-\sigma_{k+1}\left(\Phi-\Phi_{k+1}\right)\right)\right] \right\} + D_n^{sat} G\left[1-\exp\left(-\sigma_n\left(\Phi-\Phi_n\right)\right)\right] \quad (1)$$

where D corresponds to the studied disorder parameter (U normalized) and D^{sat} is the associated value at saturation, n is the number of steps, Φ_i is the threshold S_n ion fluence of the i^{th} step, and σ_i the corresponding disordering cross-section. G(x) corresponds to the Heaviside function H(x) multiplied by its argument.

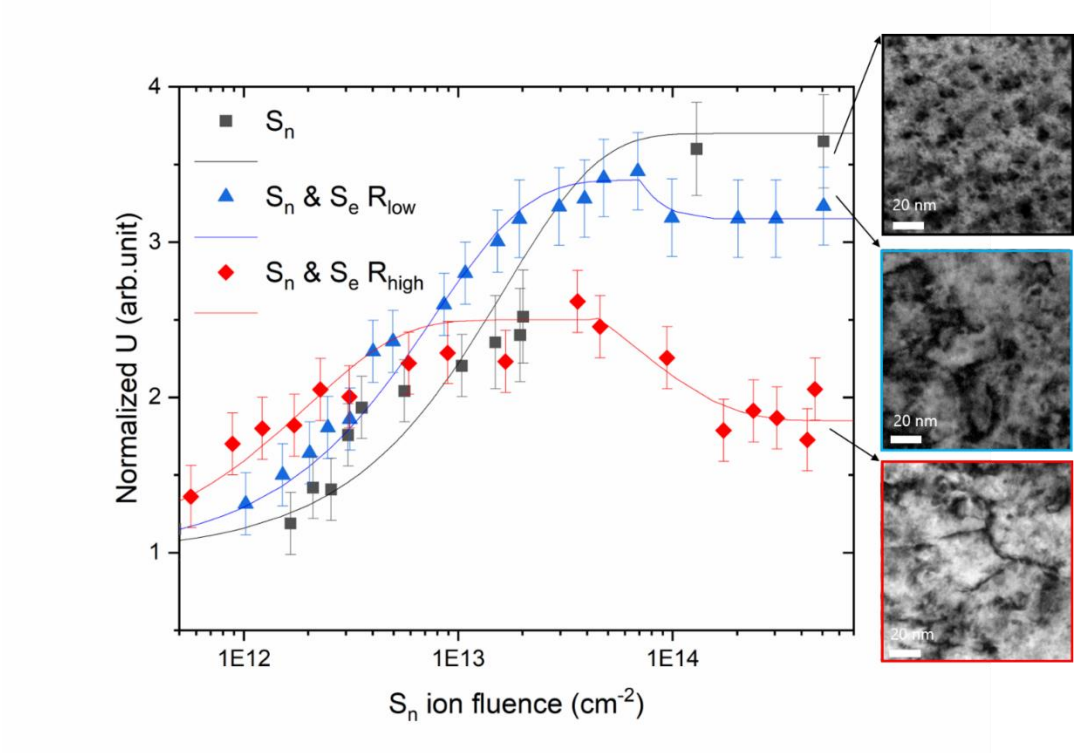

Figure 8: Damage build-up kinetics fitting by the MSDA model for UO_2 samples after the S_n, S_n & S_e R_{low} and S_n & S_e R_{high} irradiations and correlated with bright field TEM micrographs with a diffraction vector along <220>. Lines are fits of area data with Eq. (1).

For the sole S_n irradiation, the Raman signal increases then a stabilization is achieved requiring to used one step for the fitting (n=1). On contrary for the S_n & S_e irradiations, the Raman signal increases, stabilizes, and then decreases again up to a lower value, requiring two steps (n=2). The U signal is the sum of three bands area (U1, LO, and U3), so its evolution is associated with overall damage, likely linked to the accumulation of several defects. For the S_n irradiation, the increase of the Raman signal is probably linked to the small-scale defect formation. The continuous formation of point defects results in an increase of the disorder (U area). Then, a stabilization between the defect formation and their recombination, clustering or absorption by sinks occurs resulting to the non-evolution of Raman signal. During the S_n & S_e irradiations, the S_e ions induce a thermal spike along their paths activating a short-range migration of the defects. Displacement cascades are created by the S_n ions, while a recombination and an agglomeration of these defects are promoted by the electronic excitations induced by the S_e ions. Thus, the first stabilization phase occurs at lower fluence for the S_n & S_e irradiations compared to the sole S_n one, as the phenomena of clustering (resulting in the dislocation loop formation) and of recombination (reducing the local disorder) are favoured.

The second phase, only observed for the dual-beam irradiations, is more complex. Indeed, a decrease followed by a stabilization occur. The signal decrease seems to indicate that there is no longer a balance between the defect formation and their recombination/clustering. It likely reveals an increasing influence of dynamic recombination during the dual-beam irradiations. The shape of the damage build-up kinetics is similar to that obtained during a sequential irradiation (Fig. 7). In this case, electronic excitations act

on a pre-damaged microstructure (S_n + S_e). Thus, for the dual-beam irradiations (S_n & S_e), beyond a certain fluence of S_n ions, the S_e ions also interact with more extended defects, as in the case of sequential irradiation (S_n + S_e). The greater presence of extended defects coupled with the thermal spike may favour the defects recombination and defect absorption by the sinks like existing loops. This results in accelerated kinetics for the evolution of dislocation loops (Fig. 8). Thus, the greater R is, the more electronic excitations are favoured, the more the microstructure evolves.

Conclusions

The coupling between the nuclear and electronic energy losses in UO_2 was studied by single (S_n), sequential (S_n + S_e) and simultaneous (S_n & S_e) ion irradiations. The combination of *in situ* Raman spectroscopy analysis and transmission electron microscopy (TEM) observations was used to correlate the damage build-up and the dislocations evolution. These experiments unambiguously demonstrate the influence of electronic energy loss on the ballistic damage. Indeed, the S_e ions irradiation induces a microstructure evolution either after sequential or simultaneous irradiations compared to the sole S_n ions irradiations. During the sequential irradiations (S_n + S_e), the S_e ions irradiation induces a modification of the Raman spectra for the pre-damaged UO_2 samples highlighted by a decrease of the defects bands (U). The damage build-up during the S_n & S_e irradiations is different compared to the one during the sole S_n irradiation. Only an increase followed by a stabilization is observed for the S_n irradiations on contrary to the S_n & S_e irradiations, where this evolution continues with a decrease then a final stabilization. Depending on the ratio between the high- and low-velocity ion fluxes, the difference is more or less pronounced. The coupling between the displacement cascades, created by the S_n ions, and the electronic excitations, induced by the S_e ions, favours the recombination and the agglomeration of these defects. The balance between the defect formation and their recombination/clustering evolves with the ions fluence and the defect already formed in the microstructure. The phenomena of clustering (resulting in the dislocation loop formation) and of recombination (reducing the local disorder) are more or less promoted depending on the ratio between the high- and low-velocity ion fluxes. As the latter increases, electronic excitations become more favoured, leading to a greater evolution of the microstructure.

Acknowledgments

Authors acknowledge the JANNuS-Saclay facility staff for their help during the irradiations.

REFERENCES

[1] A. Debelle, G. Gutierrez, A. Boulle, F. Garrido, O. Najjar, E. Olebunne, F. Pallier, C. Cabet, L. Thomé, Disordering kinetics in monocrystalline and epitaxial Si upon energy deposition induced by dual-beam ion irradiation, Applied Physics A: Materials Science and Processing 127(10) (2021).
[2] A. Debelle, L. Thomé, I. Monnet, F. Garrido, O.H. Pakarinen, W.J. Weber, Ionization-induced thermally activated defect-annealing process in SiC, Physical Review Materials 3(6) (2019) 063609.
[3] A. Debelle, G. Gutierrez, A. Boulle, I. Monnet, L. Thomé, Effect of energy deposition on the disordering kinetics in dual-ion beam irradiated single-crystalline GaAs, Journal of Applied Physics 132(8) (2022).
[4] Y. Zhang, W.J. Weber, Ion irradiation and modification: The role of coupled electronic and nuclear energy dissipation and subsequent nonequilibrium processes in materials, Applied Physics Reviews 7(4) (2020) 041307.
[5] A.H. Mir, M. Toulemonde, C. Jegou, S. Miro, Y. Serruys, S. Bouffard, S. Peuget, Understanding and simulating the material behavior during multi-particle irradiations, Scientific Reports 6 (2016).
[6] M. Sall, I. Monnet, C. Grygiel, B. Ban d'Etat, H. Lebius, S. Leclerc, E. Balanzat, Synergy between electronic and nuclear energy losses for color center creation in AlN, EPL (Europhysics Letters) 102(2) (2013) 26002.
[7] H. Xue, E. Zarkadoula, R. Sachan, Y. Zhang, C. Trautmann, W.J. Weber, Synergistically-enhanced ion track formation in pre-damaged strontium titanate by energetic heavy ions, Acta Materialia 150 (2018) 351-359.
[8] E. Zarkadoula, K. Jin, Y. Zhang, W.J. Weber, Synergistic effects of nuclear and electronic energy loss in KTaO3 under ion irradiation, AIP Advances 7(1) (2017).
[9] C. Onofri, M. Legros, J. Léchelle, H. Palancher, C. Baumier, C. Bachelet, C. Sabathier, Full characterization of dislocations in ion-irradiated polycrystalline UO2, Journal of Nuclear Materials 494 (2017) 252-259.
[10] L.-F. He, M. Gupta, C.A. Yablinsky, J. Gan, M.A. Kirk, X.-M. Bai, J. Pakarinen, T.R. Allen, In situ TEM observation of dislocation evolution in Kr-irradiated UO2 single crystal, Journal of Nuclear Materials 443(1) (2013) 71-77.
[11] B. Ye, A. Oaks, M. Kirk, D. Yun, W.-Y. Chen, B. Holtzman, J.F. Stubbins, Irradiation effects in UO2 and CeO2, Journal of Nuclear Materials 441(1) (2013) 525-529.
[12] C. Onofri, C. Sabathier, C. Baumier, C. Bachelet, H. Palancher, B. Warot-Fonrose, M. Legros, Influence of exogenous xenon atoms on the evolution kinetics of extended defects in polycrystalline UO2 using in situ TEM, Journal of Nuclear Materials 512 (2018) 297-306.
[13] C. Sabathier, G. Martin, A. Michel, G. Carlot, S. Maillard, C. Bachelet, F. Fortuna, O. Kaitasov, E. Oliviero, P. Garcia, In-situ TEM observation of nano-void formation in UO2 under irradiation, Nuclear Instruments and Methods in Physics Research Section B: Beam Interactions with Materials and Atoms 326 (2014) 247-250.
[14] C. Onofri, C. Sabathier, G. Carlot, D. Drouan, C. Bachelet, C. Baumier, M. Gérardin, M. Bricout, Changes in voids induced by ion irradiations in UO2: In situ TEM studies, Nuclear Instruments and Methods in Physics Research Section B: Beam Interactions with Materials and Atoms 463 (2020) 76-85.
[15] N. Ishikawa, T. Sonoda, T. Sawabe, H. Sugai, M. Sataka, Electronic stopping power dependence of ion-track size in UO2 irradiated with heavy ions in the energy range of ∼1MeV/u, Nuclear Instruments and Methods in Physics Research Section B: Beam Interactions with Materials and Atoms 314 (2013) 180-184.
[16] F. Garrido, C. Choffel, J.C. Dran, L. Thome, L. Nowicki, A. Turos, Structural modifications in uranium dioxide irradiated with swift heavy ions, Nuclear Instruments and Methods in Physics Research Section B: Beam Interactions with Materials and Atoms 127-128 (1997) 634-638.
[17] T. Wiss, H. Matzke, C. Trautmann, M. Toulemonde, S. Klaumünzer, Radiation damage in UO2 by swift heavy ions, Nuclear Instruments and Methods in Physics Research Section B: Beam Interactions with Materials and Atoms 122(3) (1997) 583-588.

[18] G. Gutierrez, H. Guessous, D. Gosset, M. Bricout, I. Monnet, F. Garrido, C. Onofri, G. Adroit, A. Debelle, Defect evolution under intense electronic energy deposition in uranium dioxide, Journal of Nuclear Materials 578 (2023) 154375.
[19] M. Bricout, G. Gutierrez, C. Baumier, C. Bachelet, D. Drouan, F. Garrido, C. Onofri, Synergy of electronic and nuclear energy depositions on the kinetics of extended defects formation in UO2, based on in situ TEM observations of ion-irradiation-induced microstructure evolution, Journal of Nuclear Materials 554 (2021) 153088.
[20] M. Bricout, C. Onofri, A. Debelle, Y. Pipon, R.C. Belin, F. Garrido, F. Leprêtre, G. Gutierrez, Radiation damage in uranium dioxide: Coupled effect between electronic and nuclear energy losses, Journal of Nuclear Materials 531 (2020) 151967.
[21] G. Gutierrez, D. Gosset, M. Bricout, C. Onofri, A. Debelle, Effect of coupled electronic and nuclear energy deposition on strain and stress levels in UO2, Journal of Nuclear Materials 519 (2019) 52-56.
[22] G. Gutierrez, M. Bricout, F. Garrido, A. Debelle, L. Roux, C. Onofri, Irradiation-induced microstructural transformations in UO2 accelerated upon electronic energy deposition, Journal of the European Ceramic Society (2022).
[23] S. Pellegrino, P. Trocellier, S. Miro, Y. Serruys, É. Bordas, H. Martin, N. Chaâbane, S. Vaubaillon, J.P. Gallien, L. Beck, The JANNUS Saclay facility: A new platform for materials irradiation, implantation and ion beam analysis, Nuclear Instruments and Methods in Physics Research Section B: Beam Interactions with Materials and Atoms 273 (2012) 213-217.
[24] J.-P. Crocombette, C. Van Wambeke, Quick calculation of damage for ion irradiation: implementation in Iradina and comparisons to SRIM, EPJ Nuclear Sciences Technologies 5 (2019) 7.
[25] G. Gutierrez, C. Onofri, S. Miro, M. Bricout, F. Leprêtre, Effect of ballistic damage in UO2 samples under ion beam irradiations studied by in situ Raman spectroscopy, Nuclear Instruments and Methods in Physics Research Section B: Beam Interactions with Materials and Atoms 434 (2018) 45-50.
[26] T.R. Griffiths, H.V.S.A. Hubbard, Absorption spectrum of single-crystal UO2: Identification of and effect of temperature on the peak positions of essentially all optical transitions in the visible to near infrared regions using derivative spectroscopy, Journal of Nuclear Materials 185(3) (1991) 243-259.
[27] V.G. Keramidas, W.B. White, Raman spectra of oxides with the fluorite structure, The Journal of Chemical Physics 59(3) (1973) 1561-1562.
[28] T. Livneh, E. Sterer, Effect of pressure on the resonant multiphonon Raman scattering in UO2, Physical Review B 73(8) (2006) 085118.
[29] P. Simon, A. Canizares, N. Raimboux, L. Desgranges, How can Raman spectroscopy be used to study nuclear fuel?, MRS Bulletin (2022).
[30] T. Livneh, Resonant Raman scattering in UO2 revisited, Physical Review B 105(4) (2022) 045115.
[31] T. Livneh, Coupling of multi-LO phonons to crystal-field excitations in UO2studied by Raman spectroscopy, Journal of Physics: Condensed Matter 20(8) (2008) 085202.
[32] H. He, D. Shoesmith, Raman spectroscopic studies of defect structures and phase transition in hyper-stoichiometric UO2+x, Physical Chemistry Chemical Physics 12(28) (2010) 8109-8118.
[33] L. Desgranges, G. Guimbretière, P. Simon, C. Jegou, R. Caraballo, A possible new mechanism for defect formation in irradiated UO2, Nuclear Instruments and Methods in Physics Research Section B: Beam Interactions with Materials and Atoms 315 (2013) 169-172.
[34] R. Mohun, L. Desgranges, C. Jégou, B. Boizot, O. Cavani, A. Canizarès, F. Duval, C. He, P. Desgardin, M.F. Barthe, P. Simon, Quantification of irradiation-induced defects in UO2 using Raman and positron annihilation spectroscopies, Acta Materialia 164 (2019) 512-519.
[35] L. Desgranges, A. Canizares, P. Simon, Annealing of the Raman defect peaks in He-implanted UO2, Journal of Nuclear Materials 559 (2022) 153405.
[36] C. Onofri, C. Sabathier, C. Baumier, C. Bachelet, H. Palancher, M. Legros, Evolution of extended defects in polycrystalline Au-irradiated UO2 using in situ TEM: Temperature and fluence effects, Journal of Nuclear Materials 482 (2016) 105-113.
[37] A. Chartier, C. Onofri, L.V. Brutzel, C. Sabathier, O. Dorosh, J. Jagielski, Early stages of irradiation induced dislocations in urania, 109(18) (2016) 181902.

[38] J. Jagielski, L. Thomé, Multi-step damage accumulation in irradiated crystals, Applied Physics A 97(1) (2009) 147-155.